

2023-05

# Floating hydroelastic circular plate in regular and irregular waves

Michele, Simone

<http://hdl.handle.net/10026.1/20289>

---

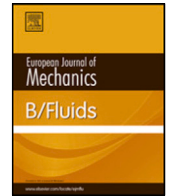
10.1016/j.euromechflu.2023.01.008

European Journal of Mechanics - B/Fluids

Elsevier

---

*All content in PEARL is protected by copyright law. Author manuscripts are made available in accordance with publisher policies. Please cite only the published version using the details provided on the item record or document. In the absence of an open licence (e.g. Creative Commons), permissions for further reuse of content should be sought from the publisher or author.*



# Floating hydroelastic circular plate in regular and irregular waves

Simone Michele, Siming Zheng\*, Federica Buriani, Alistair G.L. Borthwick, Deborah M. Greaves

University of Plymouth, School of Engineering Computing and Mathematics, Drake Circus, Plymouth, PL4 8AA, Devon, United Kingdom

## ARTICLE INFO

### Article history:

Available online 31 January 2023

### Keywords:

Fluid–structure interaction  
Floating flexible plate  
Ocean waves

## ABSTRACT

An understanding of the hydroelastic response of a flexible circular plate to water waves is relevant to many problems in ocean engineering ranging from offshore wave energy converters and solar wind devices to very large floating structures such as floating airports and ice sheets. This paper describes results from physical model tests undertaken in the COAST laboratory at the University of Plymouth. Response amplitude operators (RAOs) of a floating flexible circular disk are determined for incident monochromatic and irregular wave trains, the latter defined by JONSWAP spectra. Free-surface displacements are measured using wave gauges, and the plate motion recorded using a QUALISYS<sup>®</sup> motion tracking system. Different basin depths and plate thicknesses are considered in order to quantify the effects of water depth and flexural plate rigidity on the overall dynamic behaviour of the circular disk. We present synchronous and subharmonic nonlinear responses for monochromatic waves, and displacement spectra for irregular waves. The measured wave hydrodynamics and disk hydroelastic responses match theoretical predictions based on linear potential flow theory.

© 2023 The Author(s). Published by Elsevier Masson SAS. This is an open access article under the CC BY license (<http://creativecommons.org/licenses/by/4.0/>).

## 1. Introduction

The analysis of the fluid loading on and response of rigid and flexible plates is important in developing an understanding of many fluid–structure interaction phenomena encountered in ocean engineering, offshore renewable energy, and nature (such as ice plates in polar waters). In recent decades, there has been growing interest in the use of artificial, hydroelastic marine structures for residential, industrial, and transport purposes [1]. Very Large Floating Structures (VLFS) have been proposed for floating airports, breakwaters, bridges, piers and docks, storage facilities, recreation parks, habitation, offshore wind foundation, etc., and are essentially large, almost horizontal plates that rest on the sea surface [2,3]. Certain other artificial structures, such as flexible wave energy converters [4] and offshore solar farms [5], also comprise floating plates but are smaller than VLFS. Floating sea ice [6] is a natural plate-shaped structure found in polar waters, and is of particular relevance given the heating effect on the oceans due to global climate change.

Wave scattering by a horizontal circular plate floating on the water free surface is a classical problem in hydrodynamics that has been investigated by many researchers [7]. Miles and Gilbert

[8] considered wave diffraction by a partly immersed circular dock in water of finite depth, and reduced the problem to a Fredholm integral equation of the first kind with symmetrical kernel, from which they obtained a variational approximation to the far field. Later Garrett [9] solved the same problem by transforming the mathematical system into an infinite set of linear algebraic equations of the second kind. Black et al. [10] applied Schwinger's variational formulation to the radiation of surface waves by small-amplitude oscillations of a circular dock. Dorfmann [11] considered a circular plate lying on the water free surface, which is a limiting case of the circular dock-problem. Bennetts and Williams [12] carried out a series of physical tests on water wave transmission by an array of circular rigid floating plates in a 32 m long, 16 m wide wave basin, and found that the wave-energy transmission of the array increased monotonically with increasing wave period.

When the plate stiffness is not very large, flexural deformation of disk can significantly affect its hydroelastic response behaviour. In such cases, the simplistic assumption of rigid motion fails, and elasticity becomes a leading order effect [4]. To predict the response of a circular flexible ice floe subjected to long-crested sea waves, Meylan and Squire [6] proposed two independent theoretical techniques for a thin circular plate: one based on directly on eigenfunction expansions, the other whereby a more general method of eigenfunctions was used to construct a Green's function for the plate. Zilman and Miloh [13] derived a three-dimensional closed-form solution for water wave interaction with a floating circular thin elastic plate in shallow water.

\* Corresponding author.

E-mail addresses: [simone.michele@plymouth.ac.uk](mailto:simone.michele@plymouth.ac.uk) (S. Michele), [siming.zheng@plymouth.ac.uk](mailto:siming.zheng@plymouth.ac.uk) (S. Zheng), [federica.buriani@plymouth.ac.uk](mailto:federica.buriani@plymouth.ac.uk) (F. Buriani), [alistair.borthwick@plymouth.ac.uk](mailto:alistair.borthwick@plymouth.ac.uk) (A.G.L. Borthwick), [deborah.greaves@plymouth.ac.uk](mailto:deborah.greaves@plymouth.ac.uk) (D.M. Greaves).

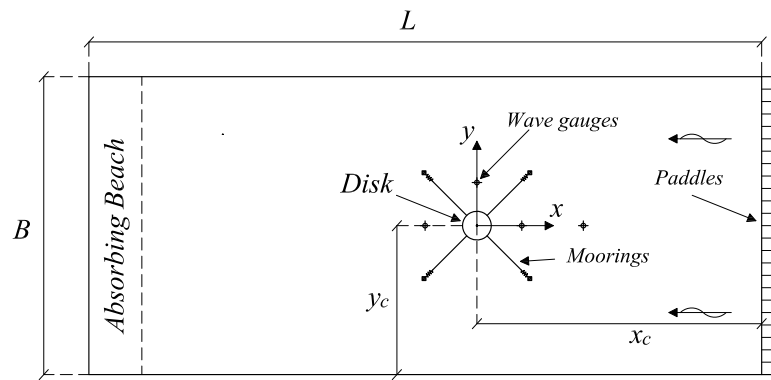


**Fig. 1.** Schematic of the plate set-up in the Ocean basin at the University of Plymouth. Crosses denote the location of the four wave gauges. Four radial lines indicate the mooring lines connected with the basin gantries.

Their solution was based on an angular eigenfunction expansion together with a dispersion equation-based method. Owing to the shallow-water approximation, this theory only required three roots of the dispersion equation in the plate-covered region. Peter et al. [14] extended this model to solve wave scattering from a circular elastic plate floating in finite-depth water, thus removing the restriction of the shallow-water approximation.

In the field of marine renewable energy, an effective way to increase wave power absorption is by means of a flexible wave energy converter (WEC) [15,16]. Michele et al. [4,17] used a dry-mode expansion to extend linear potential flow theory to flexible WECs, involving a series of power take-off units deployed under a free floating elastic plate in order to capture wave power. Recently, Zheng et al. [18] investigated wave power extraction by a circular elastic plate WEC, employing a dispersion relation-based theoretical model [19,20].

The hydroelastic characteristics of flexible plates have also been studied for an array of elastic plates [21,22], free floating and submerged circular porous elastic plates [19,23–25], time-dependent transient responses of elastic plates [26,27], and hydro-electromechanical coupled piezoelectric WECs [28,29].

Apart from the foregoing theoretical and numerical studies, a few physical model investigations have been undertaken at laboratory scale to characterise free surface wave scattering by thin elastic horizontal plates. To simulate the hydrodynamic response of idealised sea ice, Sakai and Hanai [30] conducted a series of physical tests in a 26 m long wave flume. Ultrasonic sensors were used to measure the deflection of elastic sheets at several regularly spaced locations. Recently, Brown et al. [31] analysed the 2-D hydroelastic behaviour of a floating elastic plate in a channel flume and showed that OpenFOAM models have good potential for future application to wave-driven hydroelastic problems. Montiel et al. [32,33] reported results from a series of physical tests on the flexural response of a single or pair of circular floating thin elastic plate(s) subject to monochromatic gravity waves in a 15.5 m long, 9.0 m wide, 1.9 m deep wave basin. A vertical rod was suspended through a small hole in the centre of the plate, where the frictional effects along the central rod could lead to unexpected nonlinearities, to eliminate surge and drift; and an edge barrier was introduced to prevent overtopping. Montiel et al. [32] compared the deflection data at four points of the circular plate with predictions by a numerical model. Although good overall agreement was achieved between the theoretical and experimental results, the numerical model was found consistently to overestimate the response at all wave frequencies, with a relative difference of 5%–20%. An independent experimental campaign was later conducted by Meylan et al. [34] in a 15.5 m long, 10 m wide wave basin, with a rectangular thin plastic plate used to model an ice floe. No barrier was attached

to the edge of the plate, and so waves were permitted to wash over the plate. Regular incident waves were used in their study, and the experimental data indicated that the plate's motion was essentially linear.

In this paper, we report results from physical tests in the Coastal, Ocean and Sediment Transport (COAST) laboratory at the University of Plymouth on the response of a floating hydroelastic disk in regular and irregular waves, and examine the influence of still water depth and plate flexural rigidity. Measured steady-state response amplitudes are compared against predictions by linear potential flow theory [4] (which neglects the effects of fluid viscosity and turbulence). Second and third harmonic displacements are determined in regular waves. The analysis is relevant to nonlinear WEC hydrodynamics [35–37], nonlinear ice plate modelling [38–40], and nonlinear VLFS performance [41,42]. Results are also presented for irregular waves defined by JONSWAP spectra [43] and Michele et al.'s theory [4] extended to irregular sea states. The paper is structured as follows. Section 2 describes the physical test facility and measurement instrumentation. Section 3 outlines the test programme. Section 4 presents a potential flow model for predicting the response of a horizontal circular plate to regular and irregular waves. Section 5 outlines the method used to evaluate response amplitude operators from the experimental data. Section 6 presents the experimental and theoretical results. Section 7 summarises the main findings.

## 2. Experimental set-up

Physical model tests were undertaken on a moored floating elastic disk in water waves in the COAST laboratory at the University of Plymouth. The COAST Ocean basin is of length  $L = 35$  m and width  $B = 15.5$  m, and has a movable floor that accommodates an operating depth of up to  $h = 3$  m. Water waves are generated by 24 individually controlled, hinged-flap, wave-absorbing paddles. Fig. 1 provides a schematic plan view of the basin, elastic disk, wave gauges, and mooring system. The photograph in Fig. 2 shows a perspective view of the model plate within the Ocean basin.

The origin of the coordinate system is located at the initial disk centre position,  $x$  is the horizontal axis parallel to the major basin length,  $y$  is parallel to the wavemakers, and  $z$  points vertically upwards from still water level. The origin is located a distance  $x_c = 14.8$  m from the paddles and  $y_c = 7.25$  m from each lateral wall.

The elastic disk was fabricated from expanded polyvinyl chloride (PVC) FOREX<sup>®</sup>, as also used by Montiel et al. [32] in their experiments. To avoid strong wave interactions with the lateral basin walls, the circular plate radius of  $R = 0.75$  m was selected to be much smaller than  $B$ . Two circular plates of thickness

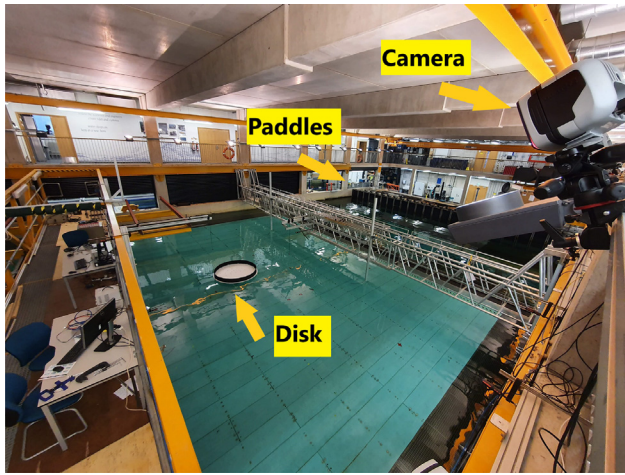


**Fig. 2.** View of the experimental set-up. The disk is placed in front of the paddles. One of the six cameras used for tracking motion is visible at the top-right of the picture.

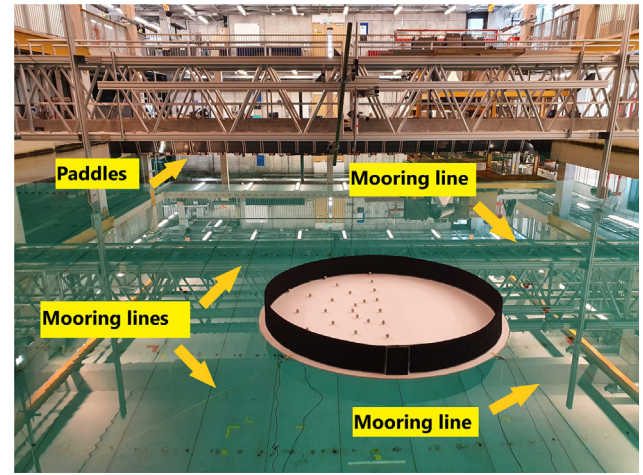


**Fig. 4.** View of elastic disk, markers, and mooring lines connected to the gantries. Each mooring line is located at  $45^\circ$  with respect to the direction of incident wave propagation  $x$ .

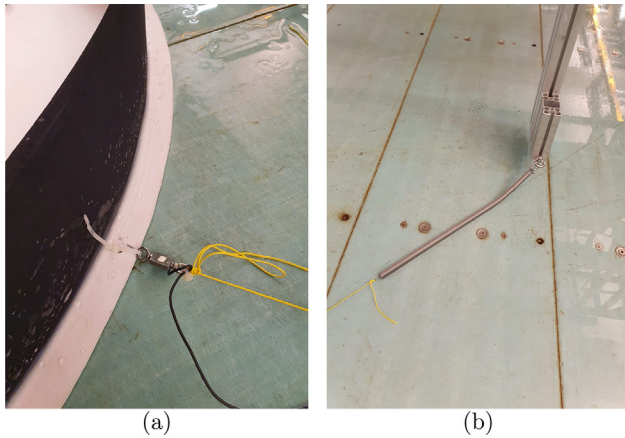


**Fig. 3.** Photograph showing connection mooring details used to avoid drift motion. The spring at the end of each mooring removed large impulsive forces.

$h_p = [3; 10]$  mm were tested in the experiments, for which we have  $h_p \ll R$ , and so our theoretical model is based on the thin plate approximation. Plate density  $\rho_p$  and Young's modulus  $E$  were evaluated experimentally because of uncertainty in the values specified by the supplier. For the 3 mm thickness plate we found  $\rho_p = 489.64 \text{ kg m}^{-3}$  and  $E = 508 \text{ GPa}$ , whereas for the 10 mm thickness plate we obtained  $\rho_p = 463.87 \text{ kg m}^{-3}$  and  $E = 854 \text{ GPa}$ . These results are very close to values reported in Table 1 of Montiel et al. [32].

To prevent second-order plate drift, we added four horizontal moorings, each of length 3 m, connected by four vertical beams fixed to the basin gantries (see Figs. 1 and 2). The vertical beams are located at  $45^\circ$  with respect to the incident wave direction, permitting symmetric response with respect to the horizontal axis  $x$ . Each mooring was fitted with a spring at its end, the spring having small stiffness  $\sim 8.73 \text{ N m}^{-1}$  to avoid impulsive forces and large vertical reactions that are not accounted for in the theoretical model. Fig. 3 shows details of the mooring connections, and Fig. 4 shows a view of the floating plate with the mooring system.

If the plate is of thickness smaller than the wave amplitude  $h_p \ll A$ , then greenwater flooding could occur. In the experiments, we fixed a black neoprene foam waterproof barrier around the edge of the plate (see Figs. 3(a) and 4) in order to avoid this

**Table 1**

Wave gauge coordinates.

	Gauge 1	Gauge 2	Gauge 3	Gauge 4
$x$ (m)	2.32	0	−2.71	5.52
$y$ (m)	0	2.245	0	0

highly nonlinear phenomenon [44] which was not included in our mathematical model. Viscous adhesive and silicon were used to prevent water filtration which could affect overall response and marker reflectivity. The neoprene had negligible stiffness and a material density of  $120 \text{ kg m}^{-3}$ , which is much smaller than that of the plates ( $489.64 \text{ kg m}^{-3}$  and  $463.87 \text{ kg m}^{-3}$ , respectively, for the 3 mm and 10 mm thickness plates), and so its contribution to plate dynamics is expected to be rather small, especially for the 10 mm thickness plate, and could be neglected.

Free-surface elevation time series were recorded using four wave gauges located in the region close to the elastic plate. The gauge locations are listed in Table 1, and indicated in Fig. 1.

Measurements were also collected in the wave basin in the absence of the plate and support structures. This facilitated measurement of the undisturbed incident wave amplitude in the disk region. With the plate present, its response amplitude operator (RAO) was then determined. Plate movement was recorded by a motion tracking device developed by QUALISYS<sup>®</sup> to an accuracy of  $O(10^{-6})$  m. A sampling frequency of 128 Hz was implemented and all the data were analysed using MATLAB. The movement measurement system comprised six infrared cameras that captured the three-dimensional positions of markers. Each marker consisted of a 30 mm diameter polystyrene sphere covered with retro-reflective tape, and glued to the top surface of the disk. The plate motion was excited by incident waves whose direction was parallel to the  $x$ -axis in order to produce a symmetric response by the disk. A total of 29 markers were fixed to the disk covering half its surface  $y \geq 0$ ; all were visible at all times by the six cameras. The markers were distributed radially in accordance with the theory described in Section 4 which is based on radial and circular eigenfrequencies.

Fig. 5(a) shows the location of the six cameras placed above the Ocean basin. Fig. 5(b) shows the marker radial distribution above the plate, whereas Fig. 6 represents the location of the 29 markers. For brevity, in the subsequent analyses, we present the oscillations recorded only by markers 0 (located at the origin), 22, 25, and 28 (located close to the neoprene barrier). Table 2 lists the coordinates of these markers.



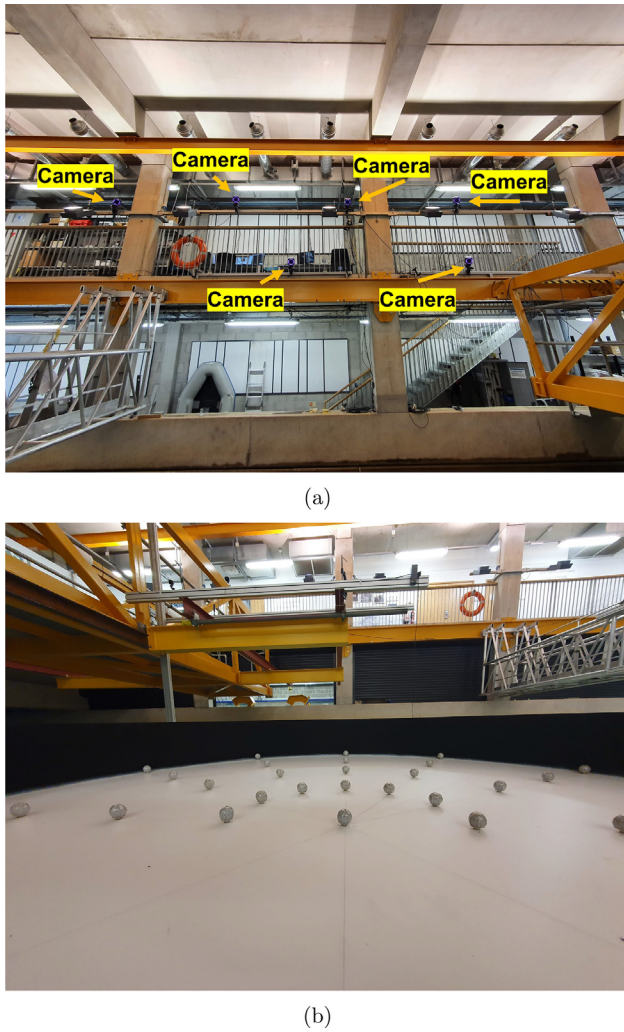


**Fig. 5.** Plate motion tracking system (a) Locations of six QUALISYS® cameras along the side wall of the Ocean basin; and (b) radial distribution of the 29 markers on the top surface of the plate.

### 3. Tests summary

Two series of tests were undertaken. The first series investigated synchronous and subharmonic plate responses to monochromatic regular waves. The second series examined the plate in irregular waves (defined according to a prescribed wave energy spectrum). The experimental results were then used to validate the theoretical model developed by Michele et al. [4] (see Section 4).

#### 3.1. Regular waves

Tests were carried out separately on two elastic disks of different thicknesses  $h_p$  in regular monochromatic waves of constant amplitude  $A$  and frequency  $f$ . Data were collected for different wave frequencies in the range  $f \in [0.4; 1.9]$  Hz with frequency increment  $\Delta f = 0.05$  Hz. Two basin depths were considered,  $h = [1.5; 3]$  m. A constant wave amplitude was selected,  $A = 0.03$  m. In the smaller depth case,  $h = 1.5$  m, measurements were recorded for a reduced wave amplitude  $A = 0.02$  m in order to investigate possible nonlinear responses that were not proportional to  $A$ . Table 3 summarises the three cases investigated for each plate thickness; for the single disk, a total of 186 tests were performed.

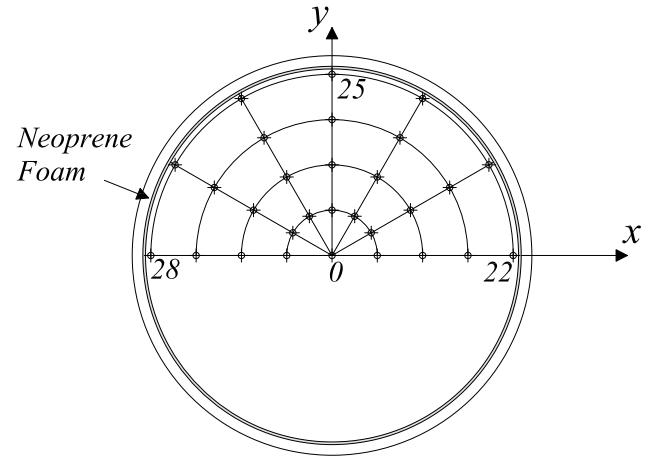


**Fig. 6.** Plan view of disk, neoprene foam barrier, and marker locations. Results from markers 0, 22, 25 and 28 are used to determine the plate dynamic behaviour.

**Table 2**

Locations of markers used in theoretical and experimental analyses.

	Marker 0	Marker 22	Marker 25	Marker 28
$x$ (m)	0	0.685	0	−0.685
$y$ (m)	0	0	0.685	0

**Table 3**

Wave amplitude  $A$  and basin depth  $h$  for the regular wave cases. Each case has been considered for each plate thickness  $h_p$ .

	Case 1	Case 2	Case 3
$A$ (cm)	3	3	2
$h$ (m)	1.5	3	1.5

#### 3.2. Irregular waves

In the second series of tests, irregular waves were defined by the JONSWAP energy spectrum  $S_\zeta$  given by Goda [43] as:

$$S_\zeta(\omega) = \frac{\alpha H_s^2}{\omega} \left( \frac{\omega_p}{\omega} \right)^4 \exp \left[ -1.25 \left( \frac{\omega_p}{\omega} \right)^4 \right] \gamma \exp \left[ -(\omega/\omega_p - 1)^2 / (2\sigma^2) \right], \quad (1)$$

in which  $H_s$  is the significant wave height,  $\omega_p = 2\pi/T_p$  denotes the peak spectral frequency,  $\omega = 2\pi f$  is the wave frequency,  $T_p$  is peak period, and

$$\alpha = \frac{0.0624(1.094 - 0.01915 \ln \gamma)}{0.23 + 0.0336\gamma - 0.185(1.9 + \gamma)^{-1}}, \quad (2)$$

$$\sigma = \begin{cases} 0.07 & : \omega \leq \omega_p \\ 0.09 & : \omega > \omega_p \end{cases}, \quad \gamma = 3.3.$$

The basin depth was fixed at  $h = 3$  m and significant wave height  $H_s = 0.04$  m to avoid possible overtopping by waves of elevation above the crest of the neoprene barrier. Five values of peak period  $T_p = [0.8; 0.9; 1.0; 1.1; 1.2]$  s were considered for each disk in order to analyse the effects of plate flexural rigidity and wave peak period on the plate response spectrum.

### 4. Mathematical model of the response of a disk to regular and irregular waves

Following Michele et al. [4] we define  $W$  as the vertical displacement of the disk above still water level and  $\Phi$  as a complex velocity potential that satisfies Laplace's equation in the fluid

domain. The system is forced by monochromatic incident waves of frequency  $\omega$ , and so we introduce the following harmonic expansion

$$\{\Phi, W\} = \text{Re} \{(\phi, w)e^{-i\omega t}\}, \quad (3)$$

where  $\phi$  is the scalar velocity potential,  $i$  is the imaginary unit, and  $t$  is time. Here, the plate undergoes symmetrical motion, oscillating through a combination of axisymmetric modes. Hence,

$$w = \zeta_h w_h + \zeta_p w_p + \sum_{m=0}^{\infty} \sum_{n=0}^{\infty} \zeta_{mn} w_{mn}, \quad (4)$$

where the first two terms represent heave and pitching, the series denote elastic bending modes, and  $\zeta_\alpha$  denotes the complex amplitude of each modal shape  $w_\alpha$ . Let  $(r, \theta)$  be radial and angular coordinates with  $\theta = 0$  corresponding with the  $x$  axis and  $\theta$  positive counterclockwise. Heave and pitch modal shapes are simply

$$w_h = 1, \quad w_p = r \cos \theta. \quad (5)$$

Elastic dry mode eigenfunctions are given by [45]

$$w_{mn} = \cos n\theta \left[ J_n \left( \frac{\lambda_{mn} r}{R} \right) - I_n \left( \frac{\lambda_{mn} r}{R} \right) T_{mn} \right], \quad (6)$$

$$n = 0, 1, \dots, \quad m = 0, 1, \dots$$

where

$$T_{mn} = \frac{J_n'' \left( \frac{\lambda_{mn} r}{R} \right) - \frac{n^2}{R^2} J_n \left( \frac{\lambda_{mn} r}{R} \right) + \frac{\nu}{R} J_n' \left( \frac{\lambda_{mn} r}{R} \right)}{I_n'' \left( \frac{\lambda_{mn} r}{R} \right) - \frac{n^2}{R^2} I_n \left( \frac{\lambda_{mn} r}{R} \right) + \frac{\nu}{R} I_n' \left( \frac{\lambda_{mn} r}{R} \right)} \Big|_{r=R}, \quad (7)$$

in which  $J_n$  and  $I_n$  are the Bessel function and modified Bessel function of order  $n$ , primes indicate the derivative with respect to the radial coordinate  $r$ ,  $\lambda_{mn}^4 = \rho_h h_p R^4 \omega_{mn}^2 / D$  is the eigenvalue, and  $\omega_{mn}$  is the relative eigenfrequency.

Following [46] we decompose the velocity potential  $\phi$  into diffraction and radiation components, i.e.

$$\phi = \phi_D + \zeta_h \phi_h + \zeta_p \phi_p + \sum_{m=0}^{\infty} \sum_{n=0}^{\infty} \zeta_{mn} \phi_{mn}, \quad \phi_D = \phi_I + \phi_S, \quad (8)$$

where the incident wave potential is

$$\phi_I = -\frac{iAg}{\omega} \sum_{n=0}^{\infty} \epsilon_n i^n J_n(k_0 r) \frac{\cosh k_0(h+z)}{\cosh k_0 h} \cos n\theta, \quad \text{in } \Omega_e, \quad (9)$$

the wavenumber  $k_0$  is the real root of the dispersion relation  $\omega^2 = gk_0 \tanh(k_0 h)$ ,  $g$  is the acceleration due to gravity,  $\phi_S$  is the scattering potential,  $\phi_D$  is the diffraction potential,  $\phi_h$  is the heaving radiation potential,  $\phi_p$  is the pitching radiation potential, and  $\phi_{mn}$  is the radiation potential related to the  $mn$ -th elastic mode.

#### 4.1. Diffraction velocity potential

The general solution for the diffraction potential beyond the disk where  $r > R$  is

$$\begin{aligned} \phi_D^{(e)} = & -\frac{iAg}{\omega} \sum_{n=0}^{\infty} \cos n\theta \left\{ \frac{\cosh k_0(h+z)}{\cosh k_0 h} \right. \\ & \times \left[ \epsilon_n i^n J_n(k_0 r) + \mathcal{A}_{0n}^D \frac{H_n^{(1)}(k_0 r)}{H_n^{(1)'}(k_0 r)} \Big|_{r=R} \right] \\ & + \sum_{l=1}^{\infty} \mathcal{A}_{ln}^D \frac{K_n(\bar{k}_l r) \cos \bar{k}_l(h+z)}{K_n'(\bar{k}_l r) \cos \bar{k}_l h} \Big|_{r=R} \Big\}, \end{aligned} \quad (10)$$

where  $\bar{k}_l$  denotes the roots of the following dispersion relation related to the evanescent components

$$\omega^2 = -g\bar{k}_l \tan \bar{k}_l h, \quad (11)$$

$H_n^{(1)}$  is the Hankel function of first kind and order  $n$ ,  $K_n$  is the modified Bessel function of second kind and order  $n$ , and  $\mathcal{A}_{ln}$  are unknown complex constants. Similarly, the solution for the diffraction potential in the fluid domain below the circular plate is given by

$$\begin{aligned} \phi_D^{(i)} = & -\frac{iAg}{\omega} \sum_{n=0}^{\infty} \cos n\theta \\ & \times \left\{ \mathcal{B}_{0n}^D \left( \frac{r}{R} \right)^n + \sum_{l=1}^{\infty} \mathcal{B}_{ln}^D \frac{I_n(\mu_l r) \cos \mu_l(h+z)}{I_n'(\mu_l r) \cos \mu_l h} \Big|_{r=R} \right\}, \quad \mu_l = \frac{l\pi}{h}, \end{aligned} \quad (12)$$

where  $\mathcal{B}_{ln}^D$  are unknown coefficients which are determined numerically as by Linton and McIver [7] and Michele et al. [4].

#### 4.2. Radiation velocity potential

The general solution in the region  $r > R$  for each radiation velocity potential  $\alpha$  is

$$\begin{aligned} \phi_\alpha^{(e)} = & \sum_{n=0}^{\infty} \cos n\theta \\ & \times \left\{ \mathcal{A}_{0n}^\alpha \frac{H_n^{(1)}(k_0 r) \cosh k_0(h+z)}{H_n^{(1)'}(k_0 r) \cosh k_0 h} \Big|_{r=R} + \sum_{l=1}^{\infty} \mathcal{A}_{ln}^\alpha \frac{K_n(\bar{k}_l r) \cos \bar{k}_l(h+z)}{K_n'(\bar{k}_l r) \cos \bar{k}_l h} \Big|_{r=R} \right\}, \end{aligned} \quad (13)$$

where the value of the subscript  $\alpha$  refers to heave, pitch, or  $mn$ th bending elastic mode. The radiation potential solution in the region below the plate where  $r < R$  is given by the homogeneous part  $\phi_\alpha^{(i)}$  in addition to a particular solution that accounts for the plate vibration. The homogeneous component is [7]

$$\begin{aligned} \phi_\alpha^{(i)} = & \sum_{n=0}^{\infty} \cos n\theta \left\{ \mathcal{B}_{0n}^\alpha \left( \frac{r}{R} \right)^n + \sum_{l=1}^{\infty} \mathcal{B}_{ln}^\alpha \frac{I_n(\mu_l r) \cos \mu_l(h+z)}{I_n'(\mu_l r) \cos \mu_l h} \right\}, \\ \mu_l = & \frac{l\pi}{h}, \end{aligned} \quad (14)$$

whereas the structure of each particular solution is independent of the others. Applying separation of variables, the particular solution for the rigid heave and pitching modes is [47]

$$\begin{aligned} \tilde{\phi}_h = & -\frac{i\omega}{2h} \left[ z^2 + 2hz - \frac{r^2}{2} \right], \\ \tilde{\phi}_p = & -\frac{i\omega r \cos \theta}{8h} [4z^2 + 8hz - r^2], \end{aligned} \quad (15)$$

and the particular solution for each bending elastic mode is

$$\begin{aligned} \tilde{\phi}_{mn} = & -i\omega R \frac{\cos n\theta}{\lambda_{mn}} \\ & \times \left\{ \frac{\cosh \frac{\lambda_{mn}(h+z)}{R} J_n \left( \frac{\lambda_{mn} r}{R} \right)}{\sinh \frac{\lambda_{mn} h}{R}} + \frac{\cos \frac{\lambda_{mn}(h+z)}{R} I_n \left( \frac{\lambda_{mn} r}{R} \right)}{\sin \frac{\lambda_{mn} h}{R}} T_{mn} \right\}, \\ n = & 0, 1, \dots \end{aligned} \quad (16)$$

As before, the unknowns  $\mathcal{A}_{ln}^\alpha$ ,  $\mathcal{B}_{ln}^\alpha$  have to be determined numerically.

#### 4.3. Plate motion

The modal amplitudes are obtained from the equation of motion of the disk. Assuming that the mooring system and neoprene foam rigidity have negligible effects, the dynamic equation can be written as

$$D\nabla^4 W + \rho_p h_p W_{tt} + \rho g W + \rho \Phi_t = 0, \quad (17)$$

where  $D = Eh_p^3/12(1-\nu^2)$  is the flexural rigidity,  $E$  is the Young's modulus of the plate material,  $\nu = 0.3$  is Poisson's ratio [32],  $\nabla^4$  denotes the biharmonic operator in cylindrical–polar coordinates,  $\rho$  is the fluid density, and the subscripts denote differentiation with respect to the relevant variable. By substituting dry mode decomposition (4) in (17) we obtain a system expressed in terms of complex modal amplitudes  $\zeta_h$ ,  $\zeta_p$  and  $\zeta_{mn}$ . The resulting linear system is then written in the following matrix form

$$\mathbf{M}\{\zeta\} = \{F\}, \quad (18)$$

where  $\mathbf{M}$  is the coefficient matrix,  $\{F\}$  is the exciting force vector, and  $\{\zeta\}$  is a vector of unknown modal amplitudes. Additional details about the numerical procedure are given by [4,7,48]. Once the complex amplitudes are evaluated, the marker displacement is simply given by substituting the coordinates in Table 2 into expression (4).

#### 4.4. Theoretical response amplitude operator for irregular incident waves

Noting that the theoretical model is based on a linear assumption, the time-dependent oscillation of the flexible disk in irregular waves can be written as [17]

$$W = \sum_{n=1}^{\infty} \sqrt{2S_{\zeta}(\omega_n) \Delta\omega} \text{RAO}(\omega_n, r, \theta) \cos(\omega_n t + \delta_n), \quad (19)$$

where  $\omega_n$  is the  $n$ th component of the discretised spectrum,  $\Delta\omega$  is the frequency interval,  $\delta_n$  is a random phase related to  $\omega_n$ , and RAO is the Response Amplitude Operator for the plate defined as

$$\text{RAO}(\omega_n, r, \theta) = \frac{|W|}{A}. \quad (20)$$

The theoretical response spectrum is consequently given by

$$S_w = S_{\zeta} \times \text{RAO}^2. \quad (21)$$

For a prescribed wave spectrum and known RAO, the response to irregular waves is given by expression (21) - used later for comparisons against the experimental results.

#### 5. Evaluation of experimental response amplitude operator

Fourier analysis was used to derive the experimental RAO from measured time-series of wave elevation and plate displacements. Following Mei [49] we assume the Fourier series expansion,

$$\eta = \frac{a_0}{2} + \sum_{n=1}^{\infty} \left( a_n \cos \left[ \frac{n\pi(2t - t_2 - t_1)}{t_2 - t_1} \right] + b_n \sin \left[ \frac{n\pi(2t - t_2 - t_1)}{t_2 - t_1} \right] \right), \quad (22)$$

where  $\eta$  refers to the recorded time series of marker or free surface vertical displacements, and the parameters  $(t_1, t_2)$  define the time interval required to reach steady state by which time transient effects become negligible. The Fourier coefficients  $a_n, b_n$

with  $n \geq 1$  represent plate oscillations and are evaluated from the integral relationships,

$$a_n = \frac{2}{t_2 - t_1} \int_{t_1}^{t_2} \eta(t) \cos \left[ \frac{n\pi(2t - t_2 - t_1)}{t_2 - t_1} \right] dt, \quad (23)$$

and

$$b_n = \frac{2}{t_2 - t_1} \int_{t_1}^{t_2} \eta(t) \sin \left[ \frac{n\pi(2t - t_2 - t_1)}{t_2 - t_1} \right] dt. \quad (24)$$

The generalised raw response amplitude spectrum is finally given by

$$\mathcal{A}_n = \sqrt{a_n^2 + b_n^2}. \quad (25)$$

### 6. Results and discussion

#### 6.1. Regular incident waves

In this Section, we analyse the synchronous and subharmonic responses of the plate by examining the RAOs of markers 0, 22, 25, and 28 for the cases listed in Table 3. Results are reported for plate thicknesses of  $h_p = 3$  mm and  $h_p = 10$  mm.

##### 6.1.1. Wave amplitude in the disk region

Water wave propagation is affected by nonlinearity, fluid viscosity, and basin geometry [46,50–53], and so the wave amplitude in the disk region might not be the same as the input assigned for wavemaker motion. Experimental values of wave amplitude  $A_{exp}(f)$  without the disk are determined by Fourier analysis of the time-series recorded by the wave gauges and averaging the  $n$ th synchronous component  $n = f(t_2 - t_1)$  of the corresponding spectrum (25). We consider a time interval of 80 s from  $t_1 = 40$  s to  $t_2 = 120$  s, during which steady state has been reached and transient effects from the initial wave front and trailing waves can be neglected [46].

Fig. 7(a) presents recorded free-surface wave amplitude versus wave frequency,  $f \in [0.4; 1.9]$  Hz, for the cases listed in Table 3. In each case, the behaviour is quite similar, with the wave amplitude declining as the wave frequency increases. This is primarily due to hydrodynamic damping. Wavemaker calibration is therefore required for the actual amplitude to match the input target value. In undertaking the comparison between experimental and theoretical RAOs in the next section, recorded values (Fig. 7(a)) are used to represent the amplitude of the forcing incident field.

The experimental wave steepness is defined as  $\epsilon = A_{exp}k$ , where  $k$  is the wavenumber satisfying the linear dispersion relation  $\omega^2 = gk \tanh(kh)$ . For  $\epsilon \ll 1$ , nonlinear quadratic and cubic products in the boundary conditions at the free-surface and plate boundaries can be neglected and the linearised leading order term is valid [46]. Nonlinear contributions are represented by second-order  $O(\epsilon)$  and third-order  $O(\epsilon^2)$  effects. In Case 1 and Case 3 the wavelengths are  $\lambda \in [8.04; 0.43]$  m. In the deeper water of Case 2 the wavelength  $\lambda \in [9.4; 0.43]$  m, and the deep water approximation can be applied at large frequencies because  $\lambda$  no longer depends on  $h$ .

Fig. 7(b) shows the rise in measured wave steepness with incident wave frequency, as the wavelength shortens. Over the range of frequencies considered,  $\epsilon < 0.27$ , i.e. much smaller than unity. This confirms the dominance of the linear contribution. Note also that at large frequencies there could be some wave breaking in the region close the wavemaker. This clearly affects wavetrain propagation and causes the wiggles for  $f > 1.6$  Hz shown in Fig. 7.

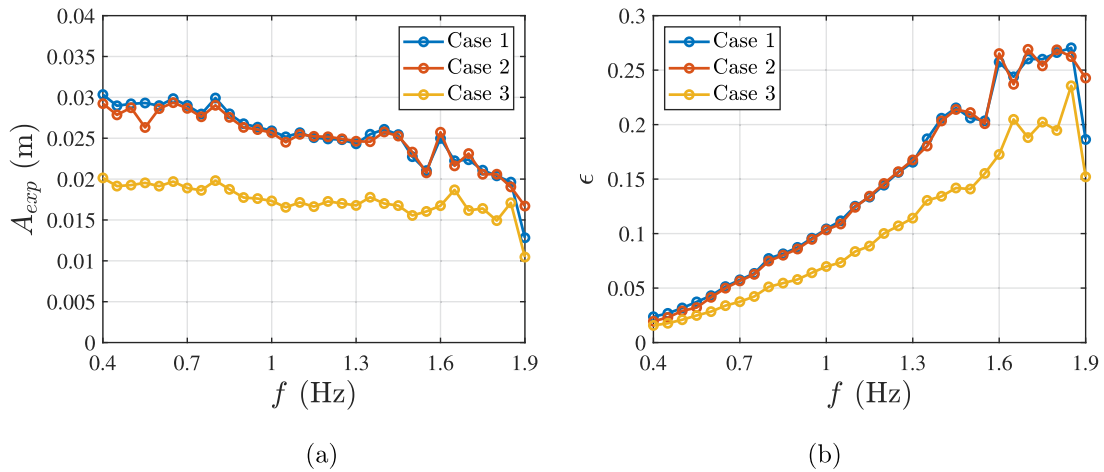


**Fig. 7.** Figure (a) recorded wave amplitude in the disk region  $A_{exp}$ , and (b) wave steepness  $\epsilon$  versus wave frequency  $f$  for cases in Table 3.

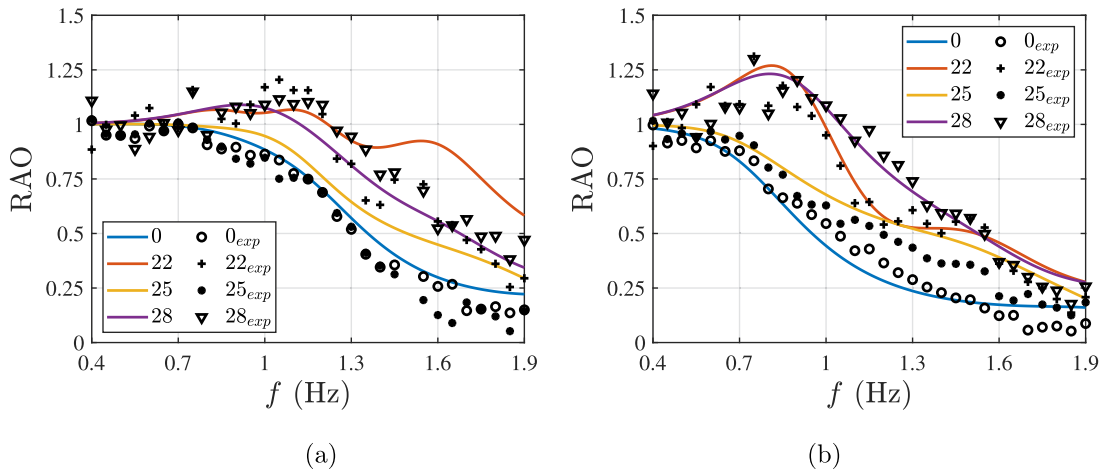


**Fig. 8.** Response amplitude operator versus frequency at marker locations 0, 22, 25 and 28 for  $h = 1.5$  m and  $A = 0.03$  m: (a)  $h_p = 3$  mm, and (b)  $h_p = 10$  mm. Solid lines depict the analytical solution whereas symbols represent the experimental results.

### 6.1.2. Synchronous linear response to monochromatic waves

We now compare theoretical predictions and experimental measurements of the plate vertical displacements. The plate response at leading order is synchronous with incident wave frequency; hence the  $n$ th component is extracted from the amplitude spectrum (25), such that  $n = f(t_2 - t_1)$ , where  $f$  is the assigned incident wave frequency. Once the  $n$ th spectrum component of marker displacements  $w_{exp}$  and wave elevation in the disk region  $A_{exp}$  have been determined, the experimental value of synchronous RAO for each marker is then evaluated using measured data from

$$RAO_{exp}(\omega) = \frac{w_{exp}}{A_{exp}}. \quad (26)$$

Consider Case 1 with basin depth  $h = 1.5$  m and incident wave amplitude  $A = 0.03$  m. Fig. 8 presents the response amplitude operator versus wave frequency for markers 0, 22, 25, and 28, and two plate thicknesses  $h_p = 3$  mm and  $h_p = 10$  mm. Bearing in mind the limitations of the theoretical model, good agreement is achieved between the theoretical RAO curve from Eq. (20) and the experimental  $RAO_{exp}$  values, especially for the larger thickness case (Fig. 8(b)). Peaks related to resonant rigid and bending modes are properly captured except

for the highest frequency peak for marker 22 in Fig. 8(a). An explanation follows. Theoretical eigenfrequency values are determined numerically by equating to zero the determinant of the coefficient matrix  $\mathbf{M}$  in Eq. (18). The first eigenfrequencies are  $f = [0.80; 1.03; 1.25; 1.43; 1.49; 1.77; 1.85]$  Hz for the 3 mm disk and  $f = [0.82; 1.06; 1.59]$  Hz for the 10 mm disk when  $h = 1.5$  m. Here, the first two values correspond to heave and pitch resonances, and depend only on plate geometry and density. The remaining eigenfrequencies relate to bending modes and thus also depend on flexural rigidity  $D$ . Hence, the theoretical model over-predicts the plate response, especially when higher bending mode resonance occurs. This occurs primarily because hydrodynamic viscous damping and viscoelastic behaviour of the disk are neglected. Even so, the mathematical model properly reproduces the experimental rigid modes and first bending mode resonance locations; this is due to the larger added mass arising from the plate motion, which reduces damping. Furthermore, the thinner the plate, the lighter and more flexible it is, making it more sensitive to the green water at the plate skirt outside the neoprene foam barrier, the effect of which is neglected in the theoretical model. In addition, the discrepancies in the theoretical results, especially for the thinner plate at high frequencies, could



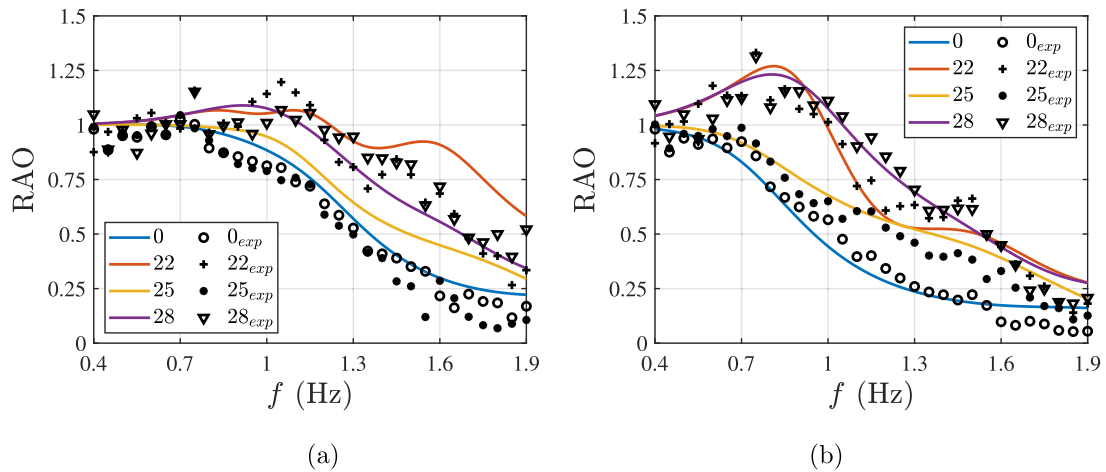


**Fig. 9.** Response amplitude operator versus frequency at marker locations 0, 22, 25 and 28 for  $h = 1.5$  m and  $A = 0.02$  m: (a)  $h_p = 3$  mm, and (b)  $h_p = 10$  mm. Solid lines depict the analytical solution whereas symbols represent the experimental results.

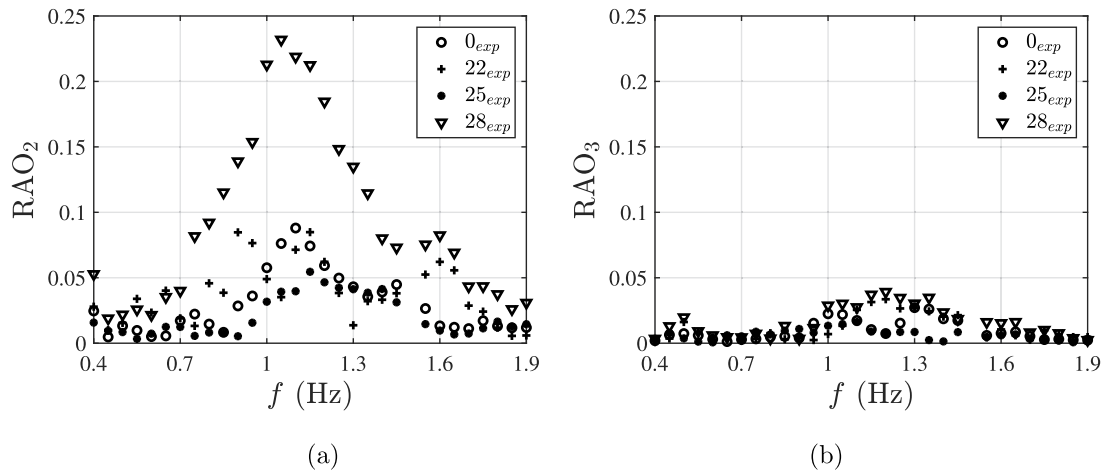


**Fig. 10.** Normalised higher harmonic response contributions versus wave frequency at marker locations 0, 22, 25 and 28 for  $h_p = 3$  mm,  $h = 1.5$  m and  $A = 0.03$  m: (a) second harmonic response  $2f$ ; and (b) third harmonic response  $3f$ .

also be due to nonlinear deformations of the plate. Indeed, a thin plate is generally rather deformable, and nonlinear effects always arise in wave tanks, even if small.

Fig. 9 compares theoretical and experimental RAO results for Case 3 where  $h = 1.5$  m and the wave amplitude is smaller,  $A = 0.02$  m. The remarkable similarity between Figs. 8 and 9 reflects the dominance of linear effects whereby the RAO does not depend strongly on  $A$ .

The results given by the Case 2 are not reported here for brevity. We anticipate that they are very similar to those in Fig. 8 because of dominant deep-water dynamics across the frequency range for  $h \geq 1.5$  m.

### 6.1.3. Second and third harmonic response

In this section, we evaluate the plate subharmonic behaviour in monochromatic waves. By following a perturbation approach, quadratic and cubic nonlinear terms are included in the boundary conditions, leading to contributions of order  $O(\epsilon)$  or smaller [46]. In the present experiments  $\epsilon \ll 1$ , and so we expect the subharmonic responses to be less pronounced than the linear synchronous behaviour. Following Mei [49], we use Fourier analysis to obtain the second harmonic  $2f$  and third harmonic  $3f$  response components to incident waves of frequency  $f$ . The components

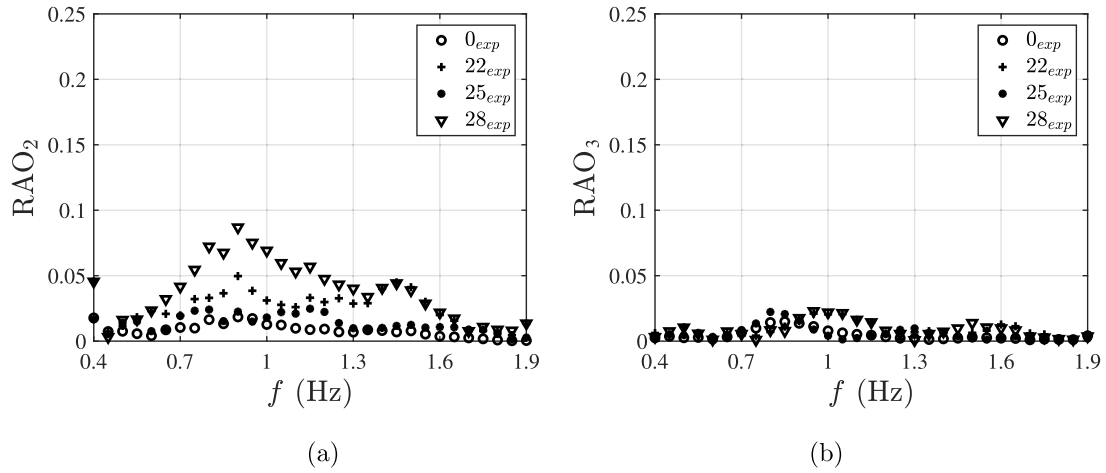
have indexes:

$$n = 2f(t_2 - t_1), \quad n = 3f(t_2 - t_1). \quad (27)$$

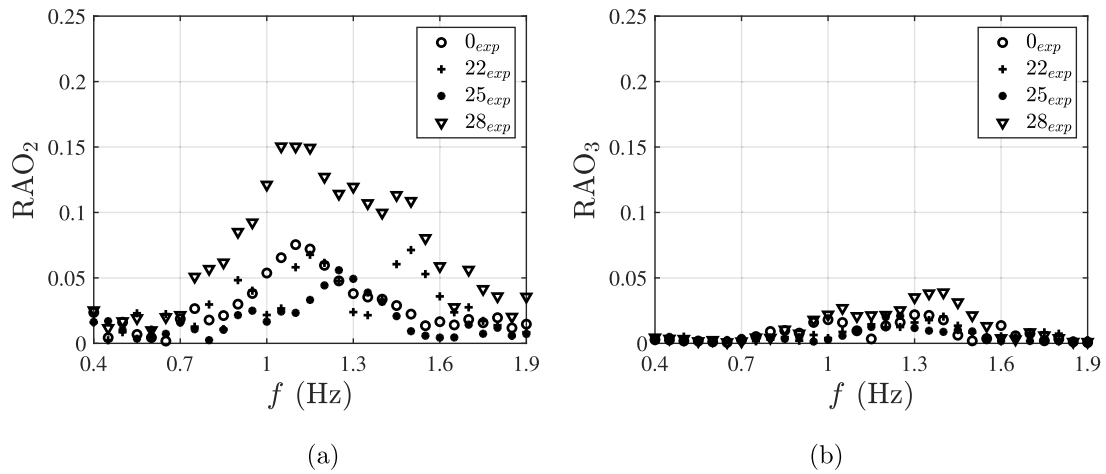
Herein, the response amplitude operators of the second and third harmonics are denoted by  $RAO_2$  and  $RAO_3$ .

Fig. 10 displays experimental subharmonic RAO according to incident wave frequency for Case 1 where  $h_p = 3$  mm,  $h = 1.5$  m, and  $A = 0.03$  m at marker locations 0, 22, 25, and 28. The subharmonic response is significantly smaller than the linear response in Fig. 8(a). This is because subharmonics are at most  $O(\epsilon)$  order effects and the wave steepness is very small in this case. Moreover, the third order harmonic response  $3f$  is much smaller than the second harmonic response  $2f$  for  $\epsilon \ll 1$ . Even so, as shown in Fig. 10(a), the second harmonic component can be important as evidenced by  $RAO_2$  approaching  $\sim 0.25$  for  $f = 1.05$  Hz. This peak, recorded at marker 28 at the back stern of the plate, warrants further theoretical investigation through weakly nonlinear approaches. We believe the peak arises from the presence of several natural bending modes in the frequency range of interest where multi-resonance is possible.

Fig. 11 depicts the subharmonic response operators when  $h_p$  is altered to 10 mm, i.e. a plate of larger thickness and flexural rigidity. The RAOs are much smaller than in the previous case,



**Fig. 11.** Normalised higher harmonic response contributions versus wave frequency at marker locations 0, 22, 25 and 28 for  $h_p = 10$  mm,  $h = 1.5$  m and  $A = 0.03$  m: (a) second harmonic response  $2f$ ; and (b) third harmonic response  $3f$ .



**Fig. 12.** Normalised higher harmonic response contributions versus wave frequency at marker locations 0, 22, 25 and 28 for  $h_p = 3$  mm,  $h = 1.5$  m and  $A = 0.02$  m: (a) second harmonic response  $2f$ ; and (b) third harmonic response  $3f$ .

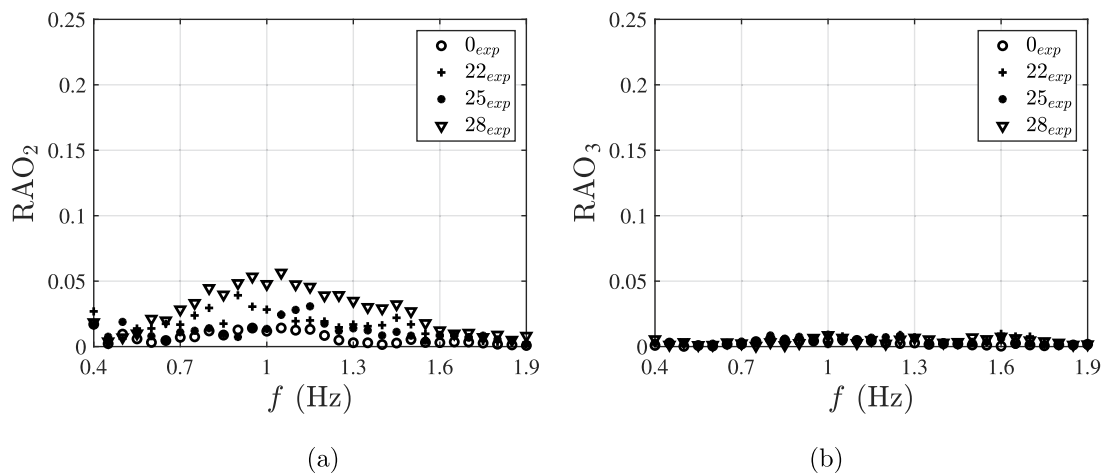


**Fig. 13.** Normalised higher harmonic response contributions versus wave frequency at marker locations 0, 22, 25 and 28 for  $h_p = 10$  mm,  $h = 1.5$  m and  $A = 0.02$  m: (a) second harmonic response  $2f$ ; and (b) third harmonic response  $3f$ .

see Fig. 10, with the second harmonic response reaching a value of  $\sim 0.1$ . Again, the plate region at the incident wave side (including marker 28) is most affected by nonlinear effects. This also warrants further investigation.

Figs. 12 and 13 show the subharmonic response for Case 3 with smaller incident wave amplitude  $A = 0.02$  m. RAO<sub>2</sub> and RAO<sub>3</sub> are overall smaller than shown in Figs. 10 and 11 because of the smaller  $A$ . Subharmonic displacements related to nonlinear

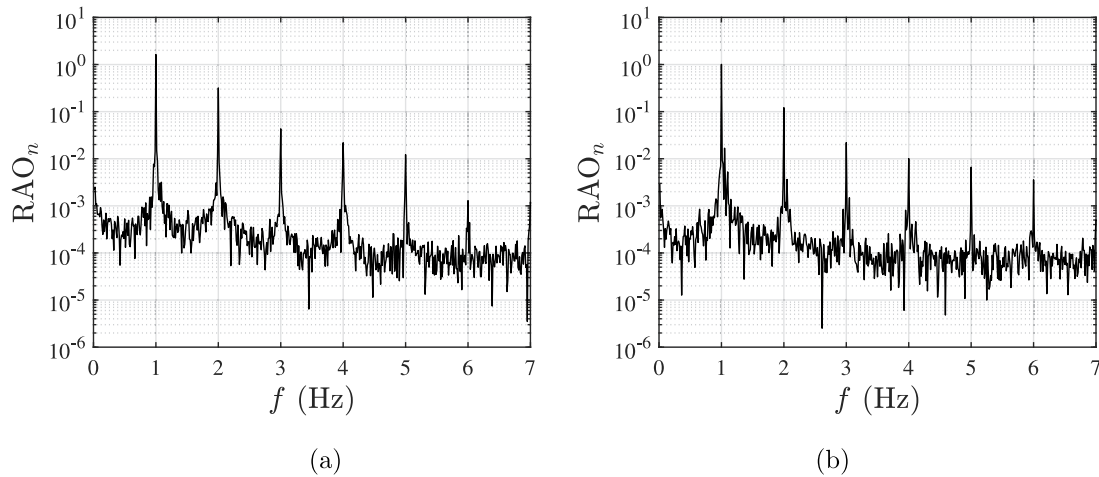


**Fig. 14.** Normalised response spectrum for incident wave frequency equal to 1 Hz,  $h_p = 3$  mm,  $h = 1.5$  m and marker 28. Figure (a)  $A = 0.03$  m; and (b)  $A = 0.02$  m.

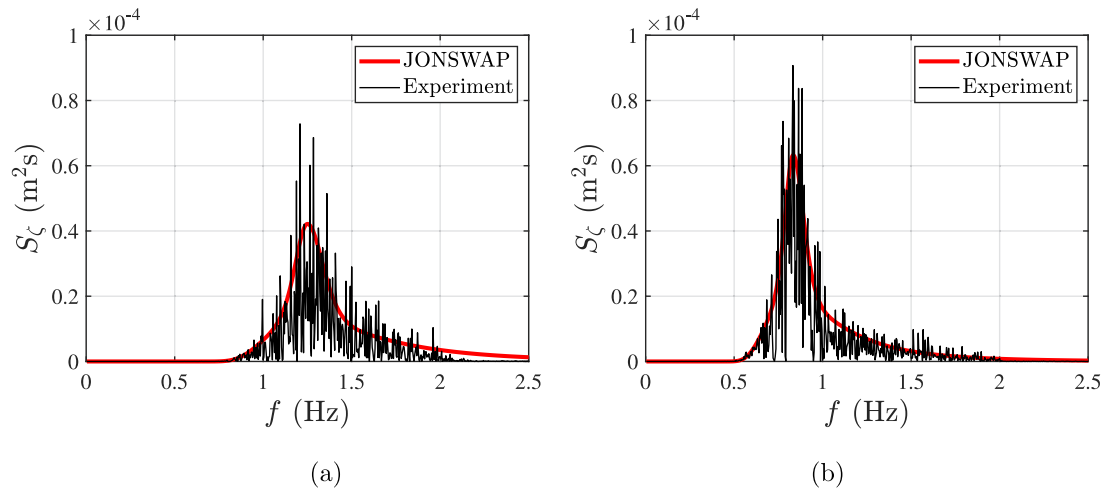


**Fig. 15.** Theoretical JONSWAP wave energy spectra prescribed by Eq. (1) and experimental wave energy spectra at wave gauge 2 without the disk present for  $H_s = 0.04$  m and peak wave period: (a)  $T_p = 0.8$  s and (b)  $T_p = 1.2$  s.

effects are therefore different to the synchronous responses in that their behaviour depends on wave amplitude.

We point out that the second and third harmonic responses for Case 2 result very similar to that in Figs. 10 and 11 respectively and are not reported here for brevity. This confirms that basin depth played a minor role for still water depth  $h \geq 1.5$  m.

To further analyse the behaviour of the subharmonic components, let us define the normalised response spectrum  $RAO_n$  as the ratio between the displacement spectrum and the synchronous component  $n = f(t_2 - t_1)$  of the incident wave spectrum. Fig. 14 shows the behaviour  $RAO_n$  of marker 28 for fixed incident wave frequency equal to 1 Hz and two wave amplitudes  $A = 0.03$  m (Case 1) and  $A = 0.02$  m (Case 3), respectively. The first peak corresponds to the synchronous RAO shown in Figs. 8(a) and 9(a), whereas the second and third peaks correspond to the subharmonic RAOs shown in Figs. 10 and 12, for  $f = 1$  Hz. Note that the larger the frequency component the smaller the corresponding peak. This is consistent with a perturbation approach in terms of wave steepness  $\epsilon$ . Furthermore, by comparing Figs. 14(a) to 14(b) we note that the response spectrum decreases with the incident wave amplitude. As already explained above,

this is due to nonlinear dependence of subharmonic components with respect to  $A_{exp}$ .

## 6.2. Irregular waves

This section considers the response of the circular hydroelastic disk to irregular waves by interpreting the disk response spectra at marker locations 0, 22, 25, and 28. Results are reported only for the two cases  $H_s = 0.04$  m and  $T_p = [0.8; 1.2]$  s.

### 6.2.1. Wave field in the region of the disk

As discussed previously for monochromatic wave generation, the actual wave amplitude is invariably somewhat different from the target input amplitude supplied to the wavemaker. For the irregular wave field, empty basin tests were necessary in order to extract the forced incident wave field. Fig. 15 shows that there is a good match between the theoretical energy spectra  $S_\zeta$  prescribed by Eq. (1) and raw experimental energy spectra of the undisturbed wave field for  $H_s = 0.04$  m and  $T_p = [0.8; 1.2]$  s.

To further investigate the behaviour of recorded  $S_\zeta$ , we evaluate the measured significant wave height from [43]

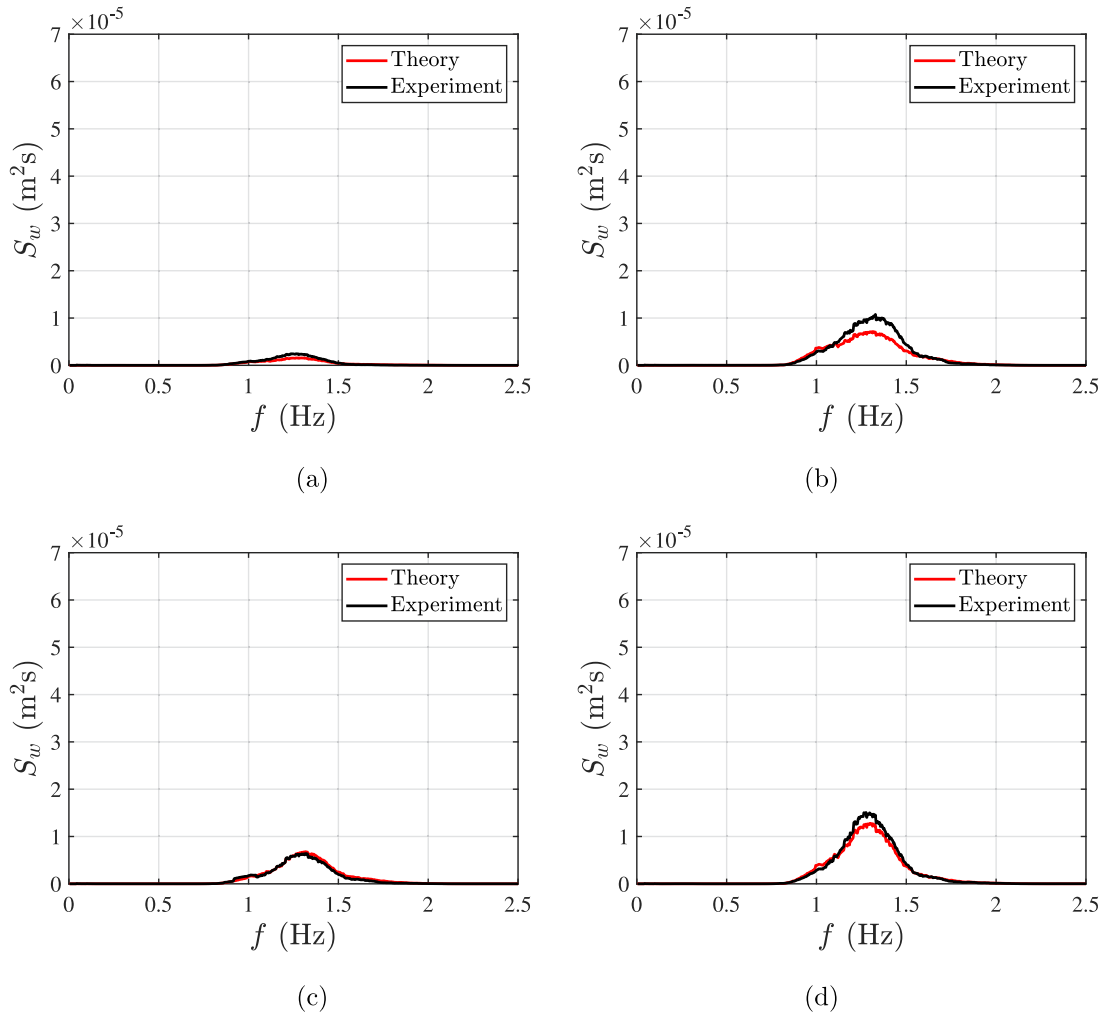


**Fig. 16.** Vertical displacement spectra for  $H_s = 0.04$  m,  $T_p = 0.8$  s and plate thickness  $h_p = 10$  mm at (a) Marker 0, (b) Marker 22, (c) Marker 25, and (d) Marker 28. The red line corresponds to theory, and the black line is obtained from the measured displacement time series. (For interpretation of the references to colour in this figure legend, the reader is referred to the web version of this article.)

$$H_{s,exp} \sim 4\sqrt{2\pi m_0}, \quad (28)$$

where  $m_0$  is the zeroth spectral moment,

$$m_0 = \int_0^\infty S_\zeta df. \quad (29)$$

By applying this expression to the data in Fig. 15 we obtain  $H_{s,exp} = [0.031; 0.033]$  m for the peak periods considered. This means that even in the case of irregular waves, the actual wave field has smaller free-surface displacements than the assigned wavemaker input  $H_s = 0.04$  m.

### 6.2.2. Response to irregular waves

We next examine disk smoothed response spectra obtained by analysing the measured vertical displacements of markers 0, 22, 25, and 28. The experimental incident wave spectra adopted for theoretical comparisons are given by the black curves shown in Fig. 15, whereas smoothing of the theoretical and experimental spectra is performed by applying the averaging method to the raw spectra  $S_w(f)$ . In this work we apply the simple rectangular smoothing and choose 31 adjacent values [43].

Figs. 16 and 17 compare the smoothed experimental and theoretical response spectra (21) obtained at each marker for  $h_p = 10$  mm and two peak periods  $T_p = [0.8; 1.2]$  s (corresponding to peak frequencies  $f_p = [1.25; 0.833]$  Hz). The theoretical model

(red lines) properly represents the experimental response (black lines) in irregular waves. The response amplitude increases with peak period because resonant heaving occurs at small frequencies close to  $f \sim 0.8$  Hz and the RAO is thus maximised.

Figs. 18 and 19 display the superimposed experimental and theoretical response spectra  $S_w$  prescribed by Eq. (21) at each marker for smaller plate thickness  $h_p = 3$  mm but the same peak periods  $T_p$  as Figs. 16 and 17. The overall agreement between the theoretical and experimental data is again very good.

For each marker, we evaluate the measured significant vertical displacement height,

$$W_s \sim 4\sqrt{2\pi \int_0^\infty S_w df}. \quad (30)$$

Table 4 summarises the theoretical and experimental significant responses obtained for each marker, peak period, and plate thickness. The agreement is very good throughout, with the maximum error having an order of magnitude of about  $O(1)$  mm. The plate response depends on marker location, having larger or smaller amplitude than the measured significant incident wave height,  $H_{s,exp} = [0.031; 0.033]$  m. In Figs. 8 and 9, the marker response amplitude operators have values that are obviously dependent on where the peak frequency is located.



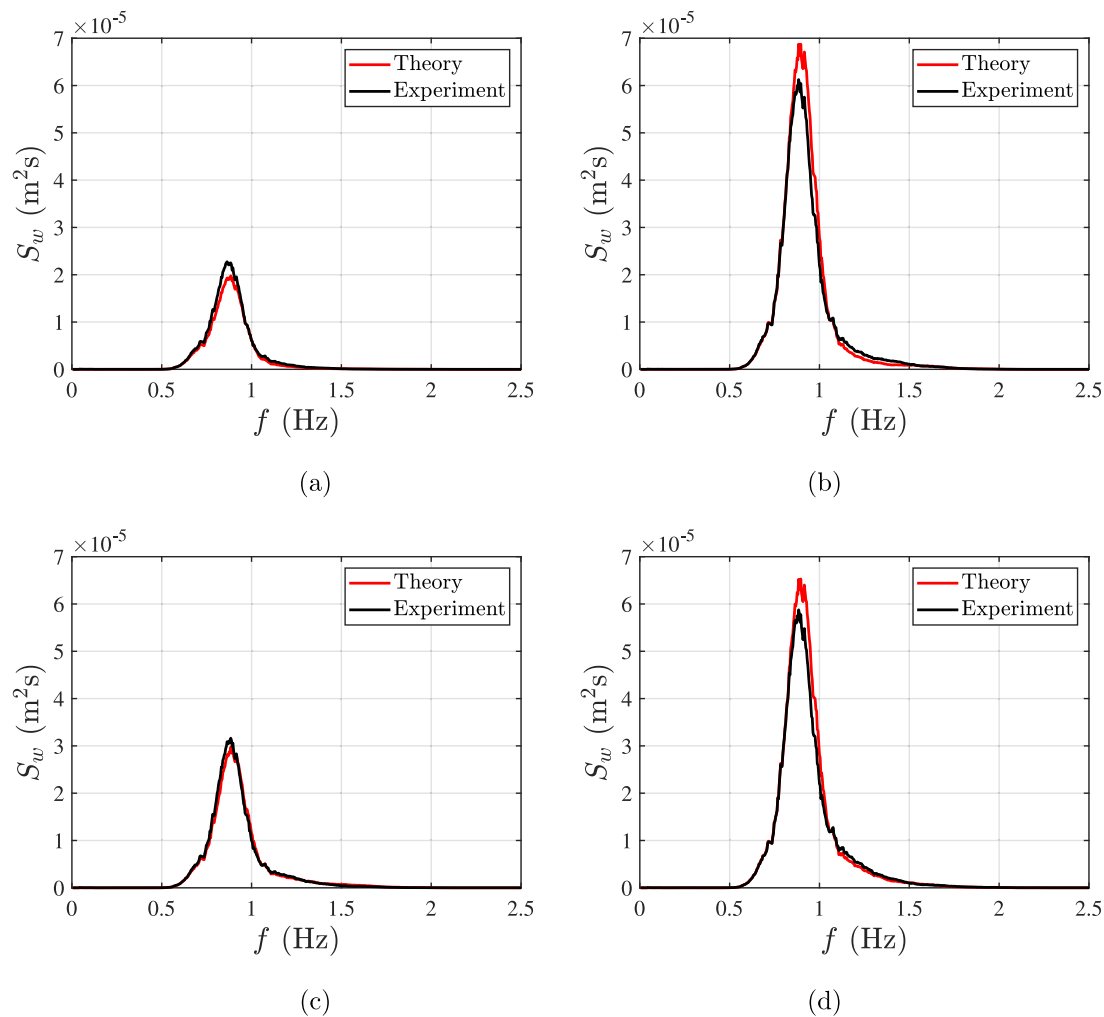


**Fig. 17.** Vertical displacement spectra for  $H_s = 0.04$  m,  $T_p = 1.2$  s and plate thickness  $h_p = 10$  mm at (a) Marker 0, (b) Marker 22, (c) Marker 25, and (d) Marker 28. The red line corresponds to theory, and the black line is obtained from the measured displacement time series. (For interpretation of the references to colour in this figure legend, the reader is referred to the web version of this article.)

**Table 4**  
Measured and theoretical significant responses  $W_s$  (m) at each marker for plate thickness  $h_p = 10$  mm and 3 mm.

		Marker 0		Marker 22		Marker 25		Marker 28	
		Measured	Theoretical	Measured	Theoretical	Measured	Theoretical	Measured	Theoretical
$h_p = 10$ mm	$T_p = 0.8$ s	0.0095	0.0083	0.0208	0.0185	0.0155	0.0161	0.0231	0.0221
	$T_p = 1.2$ s	0.0226	0.0211	0.0375	0.0388	0.0272	0.0268	0.0375	0.0390
$h_p = 3$ mm	$T_p = 0.8$ s	0.0169	0.0183	0.0275	0.0297	0.0169	0.0208	0.0263	0.0252
	$T_p = 1.2$ s	0.0294	0.0315	0.0361	0.0368	0.0304	0.0327	0.0350	0.0359

7. Conclusions

Experimental data on the hydroelastic response of a flexible circular floating plate in regular and irregular waves were obtained from physical tests conducted in the COAST laboratory at the University of Plymouth. The effect of rigid and flexible bending modes on overall disk motion was elucidated. The tests covered a wide range of wave frequencies and different still water depths and wave amplitudes. Very close agreement was obtained between experimental response spectra and their counterparts predicted using linear potential flow theory. This was particularly encouraging given the complexity of the hydroelastic problem. Some discrepancies occurred especially at large values of wave

frequency and for higher natural flexible modes. Future studies are recommended to investigate the effects of disk viscoelasticity, nonlinear wave propagation, fluid viscosity, mooring forces, and the presence of an edge barrier on plate behaviour. Using Fourier analysis, second and third sub-harmonics of the disk response were determined from the measured displacement time series. The results revealed second-order sub-harmonic resonant peaks of significant amplitude. In practice, this would cause additional internal stresses, plate deformation, and external forces on the mooring lines. Good agreement was also achieved between experimental and theoretical disk responses to irregular waves defined by JONSWAP spectra. The results support the use of potential flow theory as a tool to predict flexible body motion

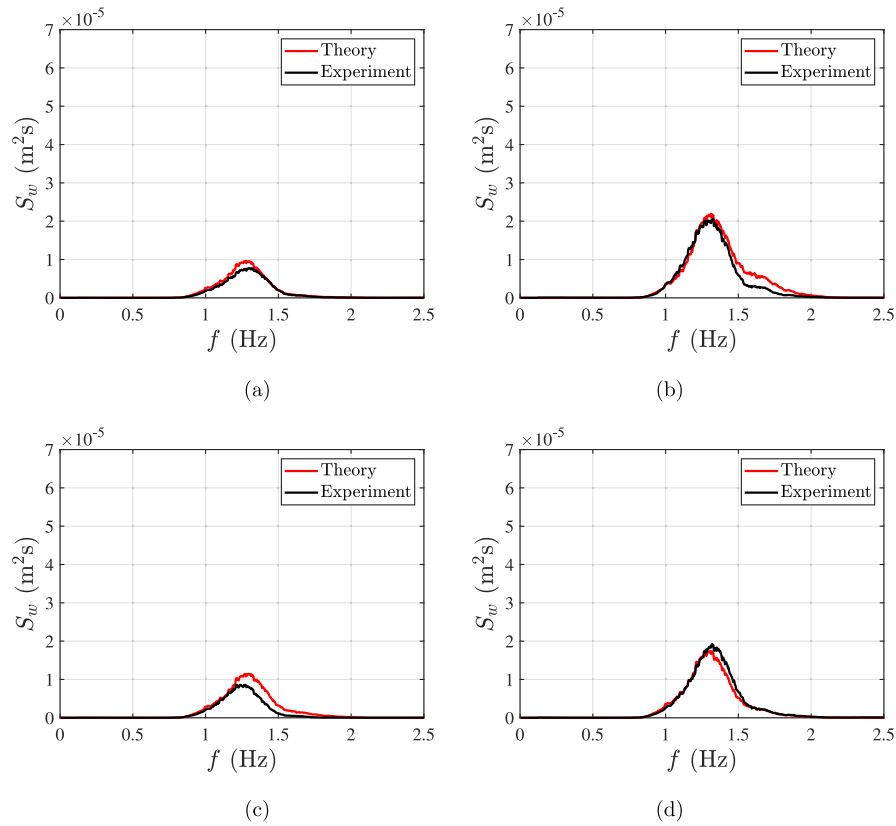


**Fig. 18.** Vertical displacement spectra for  $H_s = 0.04$  m,  $T_p = 0.8$  s and plate thickness  $h_p = 3$  mm at (a) Marker 0, (b) Marker 22, (c) Marker 25, and (d) Marker 28. The red line corresponds to theory, and the black line is obtained from the measured displacement time series. (For interpretation of the references to colour in this figure legend, the reader is referred to the web version of this article.)

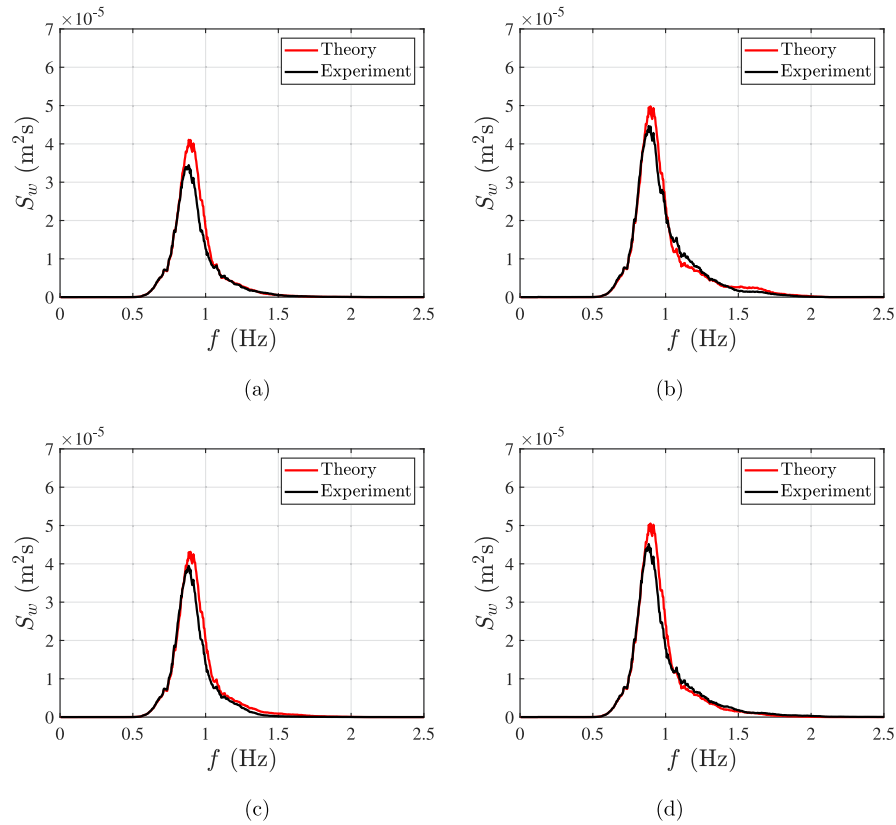


**Fig. 19.** Vertical displacement spectra for  $H_s = 0.04$  m,  $T_p = 1.2$  s and plate thickness  $h_p = 3$  mm at (a) Marker 0, (b) Marker 22, (c) Marker 25, and (d) Marker 28. The red line corresponds to theory, and the black line is obtained from the measured displacement time series. (For interpretation of the references to colour in this figure legend, the reader is referred to the web version of this article.)

in ocean water waves. The foregoing findings are relevant to the design of hydroelastic plates in offshore structures and to understanding the behaviour of ice floes.

### Declaration of competing interest

The authors declare the following financial interests/personal relationships which may be considered as potential competing interests: Simone Michele, Siming Zheng and Deborah Greaves reports financial support was provided by Supergen.

### Data availability

Data will be made available on request.

### Funding source

S.M. and S.Z. gratefully acknowledge support from the Supergen ORE Hub ECR Research Fund project ECRRF2021-12 - “Analytical and experimental modelling of a floating/submerged elastic disk”. D.G. gratefully acknowledges the EPSRC, United Kingdom for supporting part of this work through the Supergen ORE Hub, EP/S000747/1.

### References

- [1] M. Lamas-Pardo, G. Iglesias, L. Carral, A review of very large floating structures (VLFS) for coastal and offshore uses, *Ocean Eng.* 109 (2015) 677–690.
- [2] C. Wang, Z. Tay, Very large floating structures: Applications, research and development, *Procedia Eng.* 14 (2011) 62–72, The Proceedings of the Twelfth East Asia-Pacific Conference on Structural Engineering and Construction.
- [3] X. Zhang, D. Lu, Y. Liang, F. Brennan, Feasibility of very large floating structure as offshore wind foundation: Effects of hinge numbers on wave loads and induced responses, *J. Waterw. Port Coast. Ocean Eng.* 147 (2021) 0000626.
- [4] S. Michele, S. Zheng, D.M. Greaves, Wave energy extraction from a floating flexible circular plate, *Ocean Eng.* 245 (2022) 110275.
- [5] B. Bjørneklett, Offshore floating solar-a technical perspective, *PV Tech. Power.* 16 (2018) 60–64.
- [6] M.H. Meylan, V.A. Squire, Response of a circular ice floe to ocean waves, *J. Geophys. Res.* 101 (C4) (1996) 8869–8884.
- [7] C.M. Linton, P. McIver, *Mathematical Techniques for Wave/Structure Interactions*, London, UK, Chapman & Hall/CRC, 2017.
- [8] J. Miles, F. Gilbert, Scattering of gravity waves by a circular dock, *J. Fluid Mech.* 34 (1968) 783–793.
- [9] C.J.R. Garrett, Wave forces on a circular dock, *J. Fluid Mech.* 46 (1971) 129–139.
- [10] J.L. Black, C.C. Mei, M.C.G. Bray, Radiation and scattering of water waves by rigid bodies, *J. Fluid Mech.* 46 (1) (1971) 151–164.
- [11] A. Dorfmann, Water waves diffraction by a circular plate, *J. Comput. Appl. Math.* 110 (2) (1999) 287–304.
- [12] L.G. Bennetts, T.D. Williams, Water wave transmission by an array of floating discs, *Proc. R. Soc. A* 471 (2173) (2015) 20140698.
- [13] G. Zilman, T. Miloh, Hydroelastic buoyant circular plate in shallow water: a closed form solution, *Appl. Ocean Res.* 22 (2000) 191–198.
- [14] M.A. Peter, M.H. Meylan, H. Chung, Wave scattering by a circular elastic plate in water of finite depth: a closed form solution, *Int. J. Offshore Polar Eng.* 14 (2) (2004) 81–85.
- [15] E. Renzi, S. Michele, S. Zheng, S. Jin, D.M. Greaves, Niche applications and flexible devices for wave energy conversion: A review, *Energies* 14 (2021) 6537.
- [16] A. Kurniawan, J.R. Chaplin, M. Hann, D.M. Greaves, F.J.M. Farley, Wave energy absorption by a submerged air bag connected to a rigid float, *Proc. R. Soc. A* 473 (2017) 20160861.
- [17] S. Michele, F. Buriani, E. Renzi, M. van Rooij, B. Jayawardhana, A. Vakis, Wave energy extraction by flexible floaters, *Energies* 13 (2020) 6167.
- [18] S. Zheng, S. Michele, H. Liang, M. Meylan, D. Greaves, Wave power extraction from a floating elastic disk-shaped wave energy converter, *J. Fluid Mech.* 948 (2022) A38.
- [19] M.H. Meylan, L.G. Bennetts, M.A. Peter, Water-wave scattering and energy dissipation by a floating porous elastic plate in three dimensions, *Wave Motion* 70 (2017) 240–250.
- [20] S. Zheng, M.H. Meylan, G. Zhu, D.M. Greaves, G. Iglesias, Hydroelastic interaction between water waves and an array of circular floating porous elastic plates, *J. Fluid Mech.* 900 (2020) A20.
- [21] M.A. Peter, M.H. Meylan, Infinite-depth interaction theory for arbitrary floating bodies applied to wave forcing of ice floes, *J. Fluid Mech.* 500 (2004) 145–167.
- [22] L.G. Bennetts, M.A. Peter, V.A. Squire, M.H. Meylan, A three-dimensional model of wave attenuation in the marginal ice zone, *J. Geophys. Res. Oceans* 115 (C12) (2010).
- [23] S. Zheng, M.H. Meylan, D.M. Greaves, G. Iglesias, Water-wave interaction with submerged porous elastic disks, *Phys. Fluids* 32 (4) (2020) 047106.
- [24] H. Liang, S. Zheng, A. Magee, D.M. Greaves, Water wave interactions with perforated elastic disks: Quadratic pressure discharge condition, *Phys. Rev. Fluids* 7 (2022) 054802.
- [25] S. Zheng, H. Liang, S. Michele, D. Greaves, Water wave interaction with an array of submerged circular plates: Hankel transform approach, *Phys. Rev. Fluids* 8 (2023) 014803.
- [26] W. Nugroho, K. Wang, R. Hosking, F. Milinazzo, Time-dependent response of a floating flexible plate to an impulsively started steadily moving load, *J. Fluid Mech.* 381 (1999) 337–355.
- [27] F. Montiel, L.G. Bennetts, V.A. Squire, The transient response of floating elastic plates to wavemaker forcing in two dimensions, *J. Fluids Struct.* 28 (2012) 416–433.
- [28] E. Renzi, Hydroelectromechanical modelling of a piezoelectric wave energy converter, *Proc. R. Soc. A Math. Phys.* 472 (2016) 20160715.
- [29] S. Zheng, M. Meylan, X. Zhang, G. Iglesias, D.M. Greaves, Performance of a plate-wave energy converter integrated in a floating breakwater, *IET Renew. Power Gener.* 15 (14) (2021) 3206–3219.
- [30] S. Sakai, K. Hanai, Empirical formula of dispersion relation of waves in sea ice, 2002, pp. 327–335, The International Association of Hydraulic Engineering and Research.
- [31] S. Brown, N. Xie, M. Hann, D. Greaves, Investigation of wave-driven hydroelastic interactions using numerical and physical modelling approaches, *Appl. Ocean Res.* 129 (2022) 103363.
- [32] F. Montiel, F. Bonnefoy, P. Ferrant, L.G. Bennetts, V.A. Squire, P. Marsaul, Hydroelastic response of floating elastic discs to regular waves. Part 1. Wave basin experiments, *J. Fluid Mech.* 723 (2013) 604–628.
- [33] F. Montiel, L.G. Bennetts, V.A. Squire, F. Bonnefoy, P. Ferrant, Hydroelastic response of floating elastic discs to regular waves. Part 2. Modal analysis, *J. Fluid Mech.* 723 (2013) 629–652.
- [34] M.H. Meylan, L.G. Bennetts, C. Cavaliere, A. Alberello, A. Toffoli, Experimental and theoretical models of wave-induced flexure of a sea ice floe, *Phys. Fluids* 27 (4) (2015) 041704.
- [35] S. Michele, P. Sammarco, M. d’Errico, Weakly nonlinear theory for oscillating wave surge converters in a channel, *J. Fluid Mech.* 834 (2018) 55–91.
- [36] S. Michele, E. Renzi, A second-order theory for an array of curved wave energy converters in open sea, *J. Fluids Struct.* 88 (2019) 315–330.
- [37] S. Michele, E. Renzi, P. Sammarco, Weakly nonlinear theory for a gate-type curved array in waves, *J. Fluid Mech.* 869 (2019) 238–263.
- [38] E.I. Pärä, F. Dias, Nonlinear effects in the response of a floating ice plate to a moving load, *J. Fluid Mech.* 460 (2002) 281–305.
- [39] E. Dinvy, H. Kalish, E.I. Pärä, Fully dispersive models for moving loads on ice sheets, *J. Fluid Mech.* 876 (2019) 122–149.
- [40] A. Alberello, E.I. Pärä, A dissipative nonlinear Schrödinger model for wave propagation in the marginal ice zone, *Phys. Fluids* 34 (2022) 061702.
- [41] D. Xia, R. Ertekin, J. Kim, Fluid-structure interaction between a two-dimensional mat-type VLFS and solitary waves by the Green-Naghdi theory, *J. Fluids Struct.* 24 (4) (2008) 527–540.
- [42] Y. Cheng, C. Ji, G. Zhai, G. Oleg, Fully nonlinear numerical investigation on hydroelastic responses of floating elastic plate over variable depth sea-bottom, *Mar. Struct.* 55 (2017) 37–61.
- [43] Y. Goda, *Random Seas and Design of Maritime Structures*, World Scientific, Singapore, 2000.
- [44] D.M. Skene, L.G. Bennetts, M.H. Meylan, A. Toffoli, Modelling water wave overwash of a thin floating plate, *J. Fluid Mech.* 777 (2015) R3.
- [45] J.N. Reddy, *Theory and Analysis of Elastic Plates and Shells*, London, UK, CRC Press, Taylor & Francis Group, 2007.
- [46] C.C. Mei, M. Stiassnie, D.K.-P. Yue, *Theory and Application of Ocean Surface Waves*, World Scientific, Singapore, 2005.
- [47] R.W. Yeung, Added mass and damping of a vertical cylinder in finite-depth waters, *Appl. Ocean Res.* 3 (1981) 119–133.
- [48] J.N. Newman, Wave effects on deformable bodies, *Appl. Ocean Res.* 16 (1994) 47–59.

- [49] C.C. Mei, *Mathematical Analysis in Engineering*, Cambridge University Press, New York, 1997.
- [50] I. Karpadakis, C. Swan, On the average shape of the largest waves in finite water depths, *J. Phys. Oceanogr.* 50 (2020) 1023–1043.
- [51] W. Mortimer, A.C. Raby, A. Antonini, D.M. Greaves, T.S. van den Bremer, Correct generation of the bound set-down for surface gravity wave groups in laboratory experiments of intermediate to shallow depth, *Coast. Eng.* 174 (2022) 104121.
- [52] R. Calvert, C. Whittaker, A.C. Raby, P. Taylor, A.G.L. Borthwick, T.S. van den Bremer, Laboratory study of the wave-induced mean flow and set-down in unidirectional surface gravity wave packets on finite water depth, *Phys. Rev. Fluids* 4 (2019) 114801.
- [53] S. Michele, E. Renzi, A.G.L. Borthwick, C. Whittaker, A.C. Raby, Weakly nonlinear theory for dispersive waves generated by moving seabed deformation, *J. Fluid Mech.* 937 (2022) A8.